

Data report: permeability and microfabric of mud(stone) samples from IODP Sites C0011 and C0012, NanTroSEIZE subduction inputs¹

Chen Song,² Mehmet Koray Ekinci,² Michael B. Underwood,² and Pierre Henry³

Chapter contents

Abstract	1
Introduction	1
Methods and materials	2
Results	4
Acknowledgments	5
References	5
Figures	7
Tables	21
Appendix	25
Appendix figures	26

Abstract

This report documents the results of constant-flow permeability tests in the horizontal (cross-core) and vertical (along-core) directions, administered at an effective isotropic confining stress of 0.55 MPa (80 psi). The whole-round specimens of mud(stone) were collected from depths of ~34 to 748 meters below seafloor at Integrated Ocean Drilling Program Sites C0011 and C0012 in the Shikoku Basin. Unfortunately, only ten samples were tested successfully; five samples failed because of drilling-induced core damage or friability. Most test results show minor anisotropy effects, with horizontal permeability greater than vertical. At Site C0011, the range of hydraulic conductivity (K) is 1.76×10^{-8} to 3.70×10^{-10} cm/s. Intrinsic permeability (k) ranges from 1.75×10^{-17} to 3.67×10^{-19} m², and the average ratio of horizontal to vertical permeability (k_h/k_v) is 1.26. At Site C0012, values of K range from 3.80×10^{-8} to 1.69×10^{-9} cm/s. Intrinsic permeability ranges from 3.77×10^{-17} to 1.68×10^{-18} , and the average ratio of k_h/k_v is 1.58. Environmental scanning electron microscopy shows that grain fabric is random and does not vary significantly among the specimens tested. Moreover, the correlation of microfabric statistics with k_h/k_v values is not statistically significant.

Introduction

The primary objective of Integrated Ocean Drilling Program (IODP) Expedition 322 was to document the characteristics of incoming sedimentary strata and uppermost igneous basement prior to their arrival at the subduction front of the Nankai Trough (see the “Expedition 322 summary” chapter [Underwood et al., 2010]). IODP Site C0011 is located seaward of the trench on the northwest flank of Kashinosaki Knoll in the Shikoku Basin (Fig. F1), whereas Site C0012 is located near the crest of the knoll. IODP Expedition 333 returned to both sites to core previously unsampled intervals, measure temperature, and collect additional basement material (see the “Expedition 333 summary” chapter [Expedition 333 Scientists, 2012a]).

Values of intrinsic permeability (k) and hydraulic conductivity (K) for natural clay-rich sediment and shale (e.g., Neuzil, 1994; Gamage et al., 2011) typically span several orders of magnitude. This is because hydrogeological properties of fine-grained sediments and sedimentary rocks depend on many factors, some of which are in-

¹Song, C., Ekinci, M.K., Underwood, M.B., and Henry, P., 2015. Data report: permeability and microfabric of mud(stone) samples from IODP Sites C0011 and C0012, NanTroSEIZE subduction inputs. In Saito, S., Underwood, M.B., Kubo, Y., and the Expedition 322 Scientists, *Proc. IODP*, 322: Tokyo (Integrated Ocean Drilling Program Management International, Inc.). doi:10.2204/iodp.proc.322.211.2015

²Department of Geological Sciences, University of Missouri, Columbia MO 65211, USA.

Correspondence author:
UnderwoodM@missouri.edu

³Centre Européen de Recherche et d'Enseignement des Géosciences de l'Environnement, Aix-Marseille University, Europole de l'Arbois, 13545 Aix en Provence, France.



herited from the time of deposition. Grain size and shape, sorting, particle orientation, surface charges on clay particles, and fabric are important, as are the superimposed effects of burial diagenesis (e.g., Moon and Hurst, 1984; Bennett et al., 1989). Microfabric and permeability can be highly anisotropic, especially as the depth of burial increases and alignment of platy minerals becomes more uniform with respect to the orientation of maximum principal effective stress (e.g., Clennell et al., 1999; Kim et al., 1999; Bolton et al., 2000; Aplin et al., 2006). The anisotropy of permeability should follow changes in grain fabric as burial increases because pore fluids flow more easily along, rather than across, the long-axis direction of grain alignment. To quantify the hydrogeologic anisotropy of Shikoku Basin sediments, we compared horizontal (cross-core) permeability (k_h) and vertical (along-core) permeability (k_v) at the same sampling depths. These tests add to an extensive set of transect-wide hydrogeological data as part of the Nankai Trough Seismogenic Zone Experiment (e.g., Dugan and Daigle, 2011; Ekinici et al., 2011; Rowe et al., 2012; Yue et al., 2012; Dugan and Zhao, 2013; Sreaton et al., 2013).

Methods and materials

Sampling and sample handling

The whole-round (WR) specimens that we tested from Sites C0011 and C0012 consist of hemipelagic mud and mudstone with varying degrees of consolidation. Sample depths range from 36 to 748 meters below seafloor (mbsf), with the distribution covering lithostratigraphic Units I through IV (Table T1). The dips of bedding surfaces relative to the horizontal plane (Fig. F2) are as steep as 63°, as shown by nearby measurements on split core (see the “Site C0011” and “Site C0012” chapters [Expedition 322 Scientists, 2010b, 2010c] and the “Site C0011” and “Site C0012” chapters [Expedition 333 Scientists, 2012b, 2012c]). The WR samples were capped and taped in their plastic core liners on board the *D/V Chikyu*, sealed with wet sponges in aluminum vacuum bags to retard moisture loss, and stored at ~4°C until immediately prior to trimming.

To extract each specimen, the plastic core liner was cut lengthwise along two lines 180° apart using a hacksaw. Cylinders for tests in the vertical (along-core) direction were trimmed using a wire saw and soil lathe. The length after trimming was 3.15–7.11 cm and averaged 5.78 cm (Table T1), as measured by caliper to a resolution of 0.03 cm. The diameter was 3.67–6.54 cm and averaged 4.31 cm. Whenever possible, a second cylinder for tests in the horizontal (cross-core) direction was trimmed to comparable di-

mensions from material immediately below the cylinder for vertical flow. Unfortunately, most of the deeper WR specimens that were recovered by rotary core barrel (RCB) during Expedition 322 broke while trimming because of ubiquitous drilling-induced microcracks (Table T1). In other cases, the intact material was too sparse to trim two cylinders. One specimen (322-C0012A-17R-2) cracked during the test, which compromised results. Two samples (322-C0011B-3R-4 and 322-C0012A-8R-3) could not be trimmed for a horizontal flow test because of fracturing. During Expedition 333, the hydraulic piston coring system (HPCS) and the extended punch coring system (EPCS) were deployed at shallower depths, which resulted in much better core quality. Sample 333-C0011D-32X-6, however, was too friable to trim.

For most samples, we calculated values of initial (pre-test) and post-test porosity from measurements of gravimetric water content (Table T1). This was done by oven drying the trimmings at 105°C in accordance with shipboard protocols (see the “Methods” chapter [Expedition 322 Scientists, 2010a] and the “Methods” chapter [Expedition 333 Scientists, 2012a]) and by assuming 100% pore water saturation. Values of grain density were imported from shipboard measurements of the closest adjacent specimen (see the “Site C0011” and “Site C0012” chapters [Expedition 322 Scientists, 2010b, 2010c] and the “Site C0011” and “Site C0012” chapters [Expedition 333 Scientists, 2012b, 2012c]). A correction for pore water salt content was applied using

$$W_c = (M_t - M_d)/(M_d - rM_t), \quad (1)$$

where

- W_c = corrected dry weight,
- M_t = total mass of saturated specimen,
- M_d = mass of dried specimen, and
- r = salinity (permil).

For salt corrections on pretest trimmings, we assumed an average interstitial salinity value of 35‰; for post-test trimmings, we assumed a value of 25‰ to approximate the simulated seawater that was used to saturate specimens.

Constant-flow apparatus

Yue et al. (2012) provides a thorough description of the instrumentation and testing procedures for permeability at the University of Missouri (USA). To summarize, the system consists of an acrylic confining cell, a constant-flow syringe pump, one differential pressure transducer to measure hydraulic head difference between the specimen top cap and bottom cap, and an air/water interface panel for regulat-

ing the confining fluid pressure and backpressure (Fig. F3). Signals from the differential pressure transducer permit calculations of hydraulic head difference (Δh) at a precision of ± 1 cm H₂O over a range of ± 1000 cm H₂O. A digital interface also records values of effective isotropic confining stress (σ') and elapsed time. A syringe pump (KDS Scientific, Model 260) simultaneously injects and extracts pore fluid from opposite ends of the specimen. The flow pump holds one syringe (Hamilton GasTight Series 1000) to infuse pore fluid into one end, and another syringe withdraws an equal volume of fluid from the other end at the same rate. During the tests described here, volumetric flow rate (Q) ranged from 3.0×10^{-5} cm³/min to 1.0×10^{-3} cm³/min.

Backpressure saturation

Prior to our tests, all permeant lines and porous stones are saturated with simulated seawater (25 g NaCl to 1 L tap water). After placing a specimen on the pedestal, the top cap is attached, and a latex membrane is added to encase the cylinder using a vacuum membrane expander. The confining chamber is then sealed, and the cell is filled with tap water. Saturation is achieved by ramping pore-fluid backpressure to 0.48 MPa (70 psi) using the panel board (air/water interface) while also ramping the confining pressure to maintain an effective isotropic confining stress of 0.034 MPa (5 psi). The elevated backpressure is maintained for at least 24 h. We confirm saturation by increasing the confining pressure to 0.55 MPa (80 psi) and measuring the corresponding pore pressure (u) response, which yields Skempton's B -value ($B = \Delta u / \Delta \sigma$). Specimens are "saturated" if $B \geq 0.95$ (Table T1) or if a B -value < 0.95 remains constant for more than 48 h. After saturation, the cell pressure is increased to consolidate the specimen at an isotropic effective stress of 0.55 MPa. Pore water drains during consolidation from both the top and bottom of the specimen by opening valves on the confining cell. The volume of expelled pore water is measured using the backpressure pipette and monitored for equilibrium to calculate the corresponding volume change of the specimen.

Constant-flow tests

We completed 10 successful constant-flow tests on cylinders trimmed parallel to the core axis and 8 tests on cylinders trimmed perpendicular to the core axis (Table T1). The ideal protocol consists of two tests from top to bottom (denoted subsequently as a negative flow value) and two tests bottom to top (denoted as a positive flow value) (Fig. F4). We monitor the transient response from the differential pressure transducer. Unfortunately, the pressure transducer

behaved erratically during some of the tests, and after the necessary repairs were completed, those specimens had degraded too much to yield reliable replicate tests (Table T2). Plots of applied discharge velocity (v) and steady-state hydraulic gradient (i_s) allow for visual assessments of consistency and linearity (see the "Appendix"). For tests to be regarded as reliable, the coefficient of determination (R^2), calculated by least-squares linear regression of those values, must be > 0.9835 .

Data analysis

We calculated the value of hydraulic conductivity (K , in units of m/s) for each specimen using Darcy's law:

$$Q = Ki_s A = K(\Delta h_s / \Delta L)A, \quad (2)$$

where

- Q = applied volumetric flow rate (cm³/s),
- i_s = steady-state hydraulic gradient,
- Δh_s = steady-state head difference,
- ΔL = length over which head difference occurs (initial height of the specimen), and
- A = cross-sectional flow area (initial specimen area).

The corresponding value of discharge velocity is computed using: $v = Q/A$. Conversion of hydraulic conductivity to values of intrinsic permeability (k , in units of m²) takes the permeant properties into account:

$$k = (K\mu) / (\rho g), \quad (3)$$

where

- μ = viscosity of permeant at room temperature (0.001 Pa·s),
- ρ = density of permeant (1027 kg/m³), and
- g = gravitational acceleration (9.81 m/s²).

Imaging microfabric

Yue et al. (2012) provides a thorough description of the procedures used at the University of Missouri (USA) to image and characterize microfabric. To summarize, a razor blade is used to cut oriented specimens while trimming cylinders for the vertical and horizontal flow-through tests (Fig. F5). Wet, uncoated, and unfixed surfaces are imaged using an FEI Quanta 600 FEG scanning electron microscope (SEM), which operates in environmental mode (ESEM) at 30 kV with the specimen chamber pressure set at 700 Pa. Water vapor (~98% humidity) from a built-in reservoir keeps specimens from losing moisture with the cooling stage set to 2°C. We use a gaseous backscattered electron detector, spot = 3.0, and

a working distance of ~10 mm. This combination generates an imaging resolution of ~4 nm, and dimensions of the field of view are ~145 × 130 μm at 2000× magnification (Fig. F6).

The gray mode TIF images from ESEM are processed using “ImageJ” software (rsbweb.nih.gov/ij/index.html), which isolates the apparent dimensions of objects in a 2-D image. We generally count between 100 and 500 grains per image (depending on particle size) to calculate statistics for preferred grain orientation (Table T3). Each particle orientation (azimuth of the apparent long axis) is assigned to an angle between 0° and 180°. For the vertical cut surface, the core axis is oriented at 90°. Rose diagrams were constructed using “Rozeta” software (www.softpedia.com/get/Science-CAD/Rozeta.shtml), which automatically assigns azimuths to bins at 10° intervals. Cumulative frequency curves are then used to obtain graphical solutions of standard deviation (d) according to Folk and Ward (1957) statistics:

$$d = [(\phi_{84} - \phi_{16})/4] + [(\phi_{95} - \phi_5)/6.6], \quad (4)$$

where ϕ_{84} , ϕ_{16} , ϕ_{95} , and ϕ_5 represent the azimuth (in degrees) at the eighty-fourth, sixteenth, ninety-fifth, and fifth percentiles. In this context, the largest possible value of d is 72.3° (i.e., a case in which ϕ_{16} and $\phi_5 = 0^\circ$ and ϕ_{84} and $\phi_{95} = 180^\circ$). To compare each standard deviation to this maximum d value we calculate the “index of microfabric orientation”:

$$i = 1 - (d/72.3). \quad (5)$$

With random arrangements of particles, the cumulative curve is relatively flat (slope < 0.75) near the median, the value of d is >35°, and i is <0.5. As particles attain better parallel alignment, azimuths cluster more tightly, the slope of the cumulative curve steepens (slope > 1.00) near the median, the value of d is <25°, and i is >0.65 (Yue et al., 2012). The ratio of i_h to i_v permits quantitative comparison of imaging surfaces that were cut parallel and perpendicular to the core axis and allows for numerical comparisons with the anisotropy of permeability.

We tried a second method to quantify microfabric more rigorously by calculating the mean angle (α) of the angular distribution with 180°-periodic circular statistics (Fisher, 1995; Berens, 2009). First, the mean resultant vector is calculated from the summation of unit vectors representing particle orientation. The distribution of particle orientation is 180°-periodic, so the angle of the unit vector is twice the angle measured on the particle and, hence, the mean angle α is half the angle of the mean resultant vector. The resultant vector length R is between 0 and 1 and con-

stitutes a proxy for the directionality of the distribution; a value of 0 coincides with a uniform angular distribution, and a perfectly aligned distribution results in a value of 1. The probability that data reflect a uniform distribution of orientation (p-value) is then estimated from the Rayleigh test (Fisher, 1995; Berens, 2009). The mean angle α is considered significant only if the p-value is less than 0.05. Use of this statistical approach appears generally optimistic because few images display a clear fabric based upon visual assessment. We recognized weak preferred orientations on vertical sections of two samples: 333-C0012D-9H-3, 120 cm, which displays subhorizontal bedding and a mean angle of 166° (p = 0.00341), and 333-C0012C-9H-7, 51 cm, which displays steeper bedding dips and a mean angle of 53° (p = 0.0431).

Results

Table T1 summarizes values of water content and porosity for trimmings measured before and after each flow-through test. In some cases, water content decreased relative to shipboard values, and those discrepancies probably were caused by escape of moisture during shipment and storage of the WR specimens. For two specimens (322-C0012A-8R-3 and 333-C0011D-49X-5), values of porosity increased after the flow-through test. That perturbation was probably caused by expansion of water-filled microcracks after the confining pressure of 0.55 MPa was released. Each individual test result is illustrated in the “Appendix.” Table T2 shows values of volumetric flow rate, discharge velocity, steady-state head loss, steady-state hydraulic gradient, hydraulic conductivity, and intrinsic permeability for each test. Table T4 summarizes the average values of permeability for each horizontal and vertical specimen and the corresponding k_h/k_v ratio.

As also noted by Dugan and Zhao (2013), drilling and coring disturbance was both extensive and severe during Expedition 322. Consequently, permeability values for those cores should be interpreted with caution, essentially serving as upper limits on in situ permeability. At Site C0011 (flank of Kashinotsaki Knoll), the highest value of vertical hydraulic conductivity (K_v) is 1.31×10^{-8} cm/s, with $k = 1.31 \times 10^{-17}$ m². The lowest value of K_v is 3.70×10^{-10} cm/s, with $k_v = 3.67 \times 10^{-19}$ m². The highest value of horizontal hydraulic conductivity (K_h) is 1.76×10^{-8} cm/s, with $k_h = 1.75 \times 10^{-17}$ m². The lowest value of K_h is 5.06×10^{-10} cm/s, with $k_h = 5.02 \times 10^{-19}$. The ratio k_h/k_v is generally close to 1.0, ranging from 0.87 to 1.78 and averaging 1.26. Sample 322-C0011B-3R-4 yielded unusually inconsistent results for the four

replicate tests (Table T2); its average permeability value is significantly greater than averages for nearby Sample 333-C0011D-49X-5 (Table T4), and that scatter may also be a symptom of coring damage.

At Site C0012 (crest of Kashinosaki Knoll), the highest value of K_v is 3.25×10^{-8} cm/s, with a corresponding k_v of 3.23×10^{-17} m². The lowest value of vertical K_v is 1.69×10^{-9} cm/s, with $k_v = 1.68 \times 10^{-18}$ m². The highest value of K_h is 1.76×10^{-8} cm/s, with $k_h = 1.75 \times 10^{-17}$ m². The lowest value of K_h is 5.06×10^{-10} cm/s, with $k_h = 5.02 \times 10^{-19}$ m². The k_h/k_v ratio is generally close to 1.0, ranging from 0.87 to 2.82 and averaging 1.57. The largest amount of anisotropy occurs in a sample from an interval of slumping, where bedding dips are $\sim 60^\circ$.

Figure F7 illustrates how values of vertical and horizontal permeability change with depth of burial. The range of values is consistent with the test results of Dugan and Zhao (2013) and Screamon et al. (2013) over comparable depth intervals. For the most part, values of both vertical and horizontal permeability decrease with depth, but the anisotropy of permeability remains close to 1. Figure F8 displays the relation between permeability and porosity at an effective confining stress of 0.55 MPa. As expected, the test results show a systematic decrease in permeability as porosity decreases.

Figure F9 catalogs the rose diagrams of particle orientation and corresponding values for the standard deviation, index of orientation, mean angle, and resultant vector length (see Table T3 for microfabric statistics). The cumulative frequency curves are plotted on Figure F10. The standard deviation for grain orientation ranges from 48.6° to 62.5° , and the index of orientation ranges from 0.14 to 0.33. The mean angle ranges from 8.77° to 178.11° , and the resultant vector length ranges from 0.055 to 0.220. All such values are consistent with random arrangements of particles. Ratios of i_h/i_v range from ~ 0.87 to 2.82. For the majority of specimens, microfabric on the vertical cut face shows better preferred orientation than microfabric on the horizontal cut (i.e., $i_h < i_v$). No trend is apparent between the indexes of orientation and depth of burial (Fig. F11). Similarly, we see no meaningful trend in k_h/k_v vs. depth (Fig. F11). Linear regression shows that the relation between permeability anisotropy and i values is not statistically significant. Samples with higher anisotropy of permeability ($k_h/k_v > 1$) tend to display better grain alignment on the vertical cut face, but the correlation coefficient is only 0.167 for the regression between k_h/k_v and i_h/i_v . We surmise that enhanced grain alignment probably affects permeability more as

compaction progresses below the range of our sampling.

Acknowledgments

Samples were provided by the Integrated Ocean Drilling Program (IODP). We thank the Mantle Quest Japan crew, Marine Works Japan technicians, and shipboard scientists aboard *D/V Chikyu* for their assistance in acquisition of samples during Expeditions 322 and 333. Research at the University of Missouri was supported by Turkish Petroleum Cooperation (scholarship to Ekinci), the National Science Foundation (grant OCE-0751819 to Underwood), and the Consortium for Ocean Leadership (T322A58 and T333A58 to Underwood). Junhua Guo assisted with the procedures for fabric analysis.

References

- Berens, P., 2009. CircStat: a MATLAB toolbox for circular statistics. *J. Stat. Software*, 31(10):1–21. <http://www.jstatsoft.org/v31/i10>
- Bennett, R.H., Fischer, K.M., Lavoie, D.L., Bryant, W.R., and Rezak, R., 1989. Porometry and fabric of marine clay and carbonate sediments: determinants of permeability. *Mar. Geol.*, 89(1–2):127–152. doi:10.1016/0025-3227(89)90030-3
- Bolton, A.J., Maltman, A.J., and Fisher, Q., 2000. Anisotropic permeability and bimodal pore-size distributions of fine-grained marine sediments. *Mar. Pet. Geol.*, 17(6):657–672. doi:10.1016/S0264-8172(00)00019-2
- Clennell, M.B., Dewhurst, D.N., Brown, K.M., and Westbrook, G.K., 1999. Permeability anisotropy of consolidated clays. In Aplin, A.C., Fleet, A.J., and MacQuaker, J.H.S. (Eds.), *Muds and Mudstones: Physical and Fluid-Flow Properties*. Geol. Soc. Spec. Publ., 158(1):79–96. doi:10.1144/GSL.SP.1999.158.01.07
- Dugan, B., and Daigle, H., 2011. Data report: permeability, compressibility, stress state, and grain size of shallow sediments from Sites C0004, C0006, C0007, and C0008 of the Nankai accretionary complex. In Kinoshita, M., Tobin, H., Ashi, J., Kimura, G., Lallemand, S., Screamon, E.J., Curewitz, D., Masago, H., Moe, K.T., and the Expedition 314/315/316 Scientists, *Proc. IODP*, 314/315/316: Tokyo (Integrated Ocean Drilling Program Management International, Inc.). doi:10.2204/iodp.proc.314315316.208.2011
- Dugan, B., and Zhao, X., 2013. Data report: permeability of sediments from Sites C0011 and C0012, NanTroSEIZE Stage 2: subduction inputs. In Saito, S., Underwood, M.B., Kubo, Y., and the Expedition 322 Scientists, *Proc. IODP*, 322: Tokyo (Integrated Ocean Drilling Program Management International, Inc.). doi:10.2204/iodp.proc.322.208.2013
- Ekinci, M.K., Likos, W.J., Underwood, M.B., and Guo, J., 2011. Data report: permeability of mud(stone) samples

- from IODP Sites C0006 and C0007, Nankai Trough Seismogenic Zone Experiment. *In* Kinoshita, M., Tobin, H., Ashi, J., Kimura, G., Lallemand, S., Screaton, E.J., Curewitz, D., Masago, H., Moe, K.T., and the Expedition 314/315/316 Scientists, *Proc. IODP*, 314/315/316: Washington, DC (Integrated Ocean Drilling Program Management International, Inc.). [doi:10.2204/iodp.proc.314315316.214.2011](https://doi.org/10.2204/iodp.proc.314315316.214.2011)
- Expedition 322 Scientists, 2010a. Methods. *In* Saito, S., Underwood, M.B., Kubo, Y., and the Expedition 322 Scientists, *Proc. IODP*, 322: Tokyo (Integrated Ocean Drilling Program Management International, Inc.). [doi:10.2204/iodp.proc.322.102.2010](https://doi.org/10.2204/iodp.proc.322.102.2010)
- Expedition 322 Scientists, 2010b. Site C0011. *In* Saito, S., Underwood, M.B., Kubo, Y., and the Expedition 322 Scientists, *Proc. IODP*, 322: Tokyo (Integrated Ocean Drilling Program Management International, Inc.). [doi:10.2204/iodp.proc.322.103.2010](https://doi.org/10.2204/iodp.proc.322.103.2010)
- Expedition 322 Scientists, 2010c. Site C0012. *In* Saito, S., Underwood, M.B., Kubo, Y., and the Expedition 322 Scientists, *Proc. IODP*, 322: Tokyo (Integrated Ocean Drilling Program Management International, Inc.). [doi:10.2204/iodp.proc.322.104.2010](https://doi.org/10.2204/iodp.proc.322.104.2010)
- Expedition 333 Scientists, 2012a. Expedition 333 summary. *In* Henry, P., Kanamatsu, T., Moe, K., and the Expedition 333 Scientists, *Proc. IODP*, 333: Tokyo (Integrated Ocean Drilling Program Management International, Inc.). [doi:10.2204/iodp.proc.333.101.2012](https://doi.org/10.2204/iodp.proc.333.101.2012)
- Expedition 333 Scientists, 2012b. Methods. *In* Henry, P., Kanamatsu, T., Moe, K., and the Expedition 333 Scientists, *Proc. IODP*, 333: Tokyo (Integrated Ocean Drilling Program Management International, Inc.). [doi:10.2204/iodp.proc.333.102.2012](https://doi.org/10.2204/iodp.proc.333.102.2012)
- Expedition 333 Scientists, 2012c. Site C0011. *In* Henry, P., Kanamatsu, T., Moe, K., and the Expedition 333 Scientists, *Proc. IODP*, 333: Tokyo (Integrated Ocean Drilling Program Management International, Inc.). [doi:10.2204/iodp.proc.333.104.2012](https://doi.org/10.2204/iodp.proc.333.104.2012)
- Expedition 333 Scientists, 2012d. Site C0012. *In* Henry, P., Kanamatsu, T., Moe, K., and the Expedition 333 Scientists, *Proc. IODP*, 333: Tokyo (Integrated Ocean Drilling Program Management International, Inc.). [doi:10.2204/iodp.proc.333.105.2012](https://doi.org/10.2204/iodp.proc.333.105.2012)
- Fisher, N.I., 1995. *Statistical Analysis of Circular Data*: New York (Cambridge Univ.y Press).
- Folk, R.L., and Ward, W.C., 1957. Brazos River bar [Texas]: a study in the significance of grain size parameters. *J. Sediment. Res.*, 27(1):3–26. <http://jsedres.sepmonline.org/cgi/content/abstract/27/1/3>
- Gamage, K., Screaton, E., Bekins, B., and Aiello, I., 2011. Permeability–porosity relationships of subduction zone sediments. *Mar. Geol.*, 279(1–4):19–36. [doi:10.1016/j.margeo.2010.10.010](https://doi.org/10.1016/j.margeo.2010.10.010)
- Kim, J.-W., Bryant, W.R., Watkins, J.S., and Tieh, T.T., 1999. Electron microscopic observations of shale diagenesis, offshore Louisiana, USA, Gulf of Mexico. *Geo-Mar. Lett.*, 18(3):234–240. [doi:10.1007/s003670050073](https://doi.org/10.1007/s003670050073)
- Moon, C.F., and Hurst, C.W., 1984. Fabrics of muds and shales: an overview. *In* Stow, D.A.V., and Piper, D.J.W. (Eds.), *Fine-Grained Sediments: Deep-Water Processes and Facies*. Geol. Soc. Spec. Publ., 15(1):579–593. [doi:10.1144/GSL.SP.1984.015.01.36](https://doi.org/10.1144/GSL.SP.1984.015.01.36)
- Neuzil, C.E., 1994. How permeable are clays and shales? *Water Resour. Res.*, 30(2):145–150. [doi:10.1029/93WR02930](https://doi.org/10.1029/93WR02930)
- Rowe, K.T., Screaton, E.J., and Ge, S., 2012. Coupled fluid flow and deformation modeling of the frontal thrust region of the Kumano Basin transect, Japan: implications for fluid pressures and décollement downstepping. *Geochem., Geophys., Geosyst.*, 13:Q0AD23. [doi:10.1029/2011GC003861](https://doi.org/10.1029/2011GC003861)
- Screaton, E., Rowe, K., Sutton, J., and Atalan, G., 2013. Data report: permeabilities of Expedition 322 and 333 sediments from offshore the Kii Peninsula, Japan. *In* Saito, S., Underwood, M.B., Kubo, Y., and the Expedition 322 Scientists, *Proc. IODP*, 322: Tokyo (Integrated Ocean Drilling Program Management International, Inc.). [doi:10.2204/iodp.proc.322.210.2013](https://doi.org/10.2204/iodp.proc.322.210.2013)
- Underwood, M.B., Saito, S., Kubo, Y., and the Expedition 322 Scientists, 2010. Expedition 322 summary. *In* Saito, S., Underwood, M.B., Kubo, Y., and the Expedition 322 Scientists, *Proc. IODP*, 322: Tokyo (Integrated Ocean Drilling Program Management International, Inc.). [doi:10.2204/iodp.proc.322.101.2010](https://doi.org/10.2204/iodp.proc.322.101.2010)
- Yue, L., Likos, W.J., Guo, J., and Underwood, M.B., 2012. Data report: permeability of mud(stone) samples from Site C0001, IODP Expedition 315, Nankai Trough: NanTroSEIZE Stage 1. *In* Kinoshita, M., Tobin, H., Ashi, J., Kimura, G., Lallemand, S., Screaton, E.J., Curewitz, D., Masago, H., Moe, K.T., and the Expedition 314/315/316 Scientists, *Proc. IODP*, 314/315/316: Washington, DC (Integrated Ocean Drilling Program Management International, Inc.). [doi:10.2204/iodp.proc.3314315316.204.2012](https://doi.org/10.2204/iodp.proc.3314315316.204.2012)

Initial receipt: 11 November 2013

Acceptance: 4 February 2015

Publication: 6 April 2015

MS 322-211

Figure F1. Map of NanTroSEIZE study area with locations of Sites C0011 and C0012 (modified from Expedition 333 Scientists, 2012a). White dots = other drill sites along the Kumano transect.

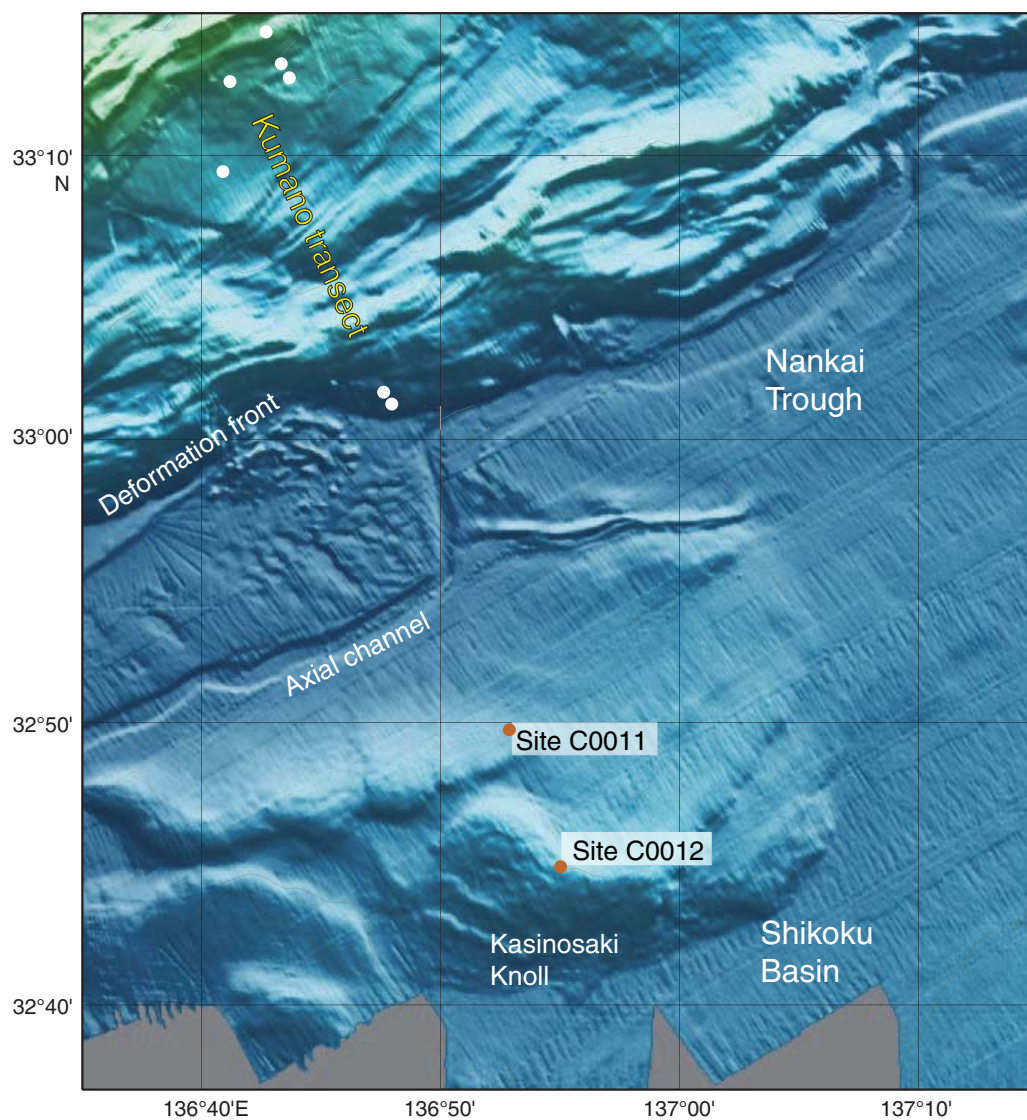


Figure F2. Stratigraphic columns and lithologic units for Sites C0011 and C0012, with positions of samples used for permeability tests. Red dots = successful tests, yellow dots = specimens that failed during trimming or testing. Bedding dips for closest nearby intervals are as previously reported (Expedition 322 Scientists, 2010b, 2010c; Expedition 333 Scientists, 2012c, 2012d).

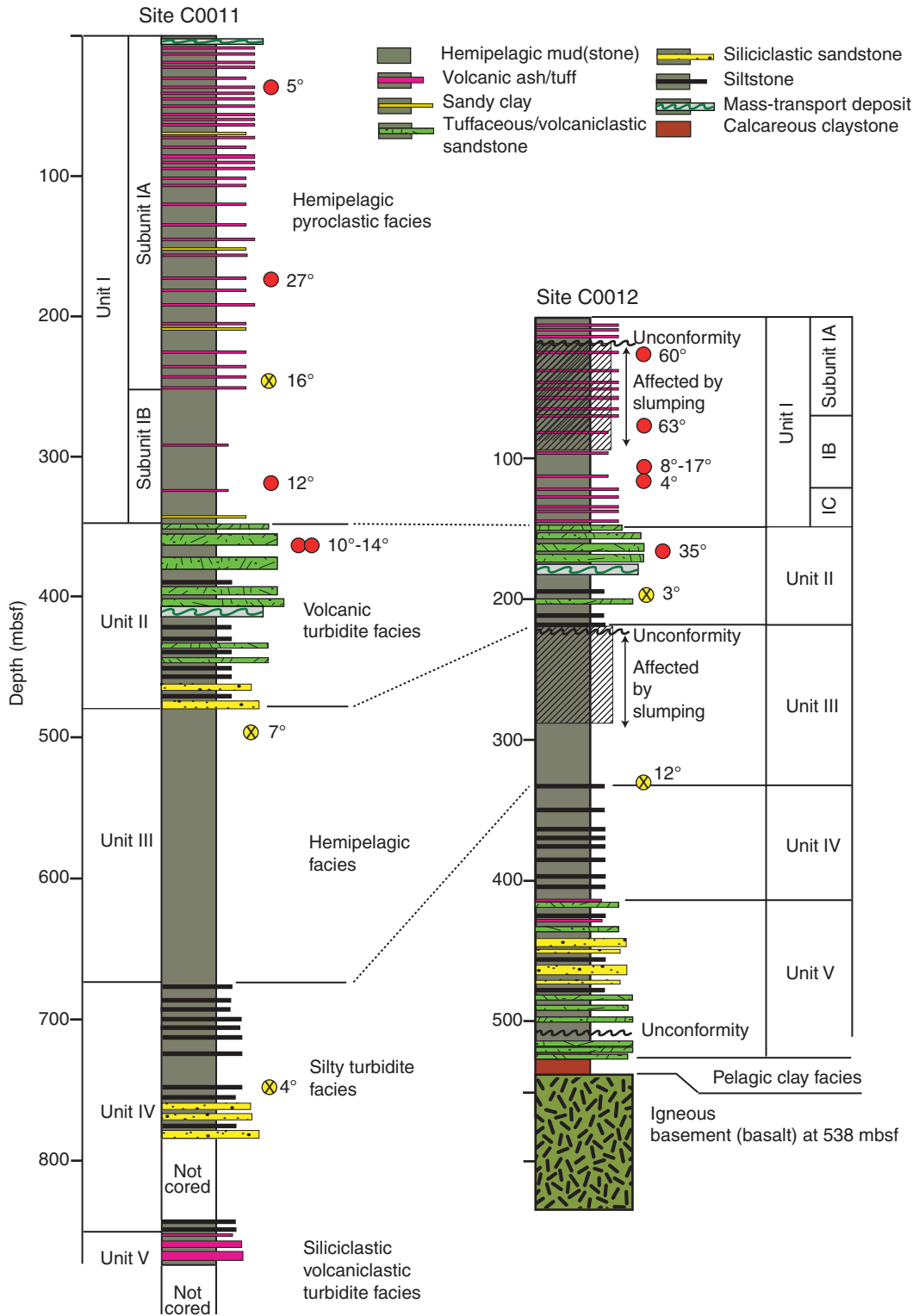


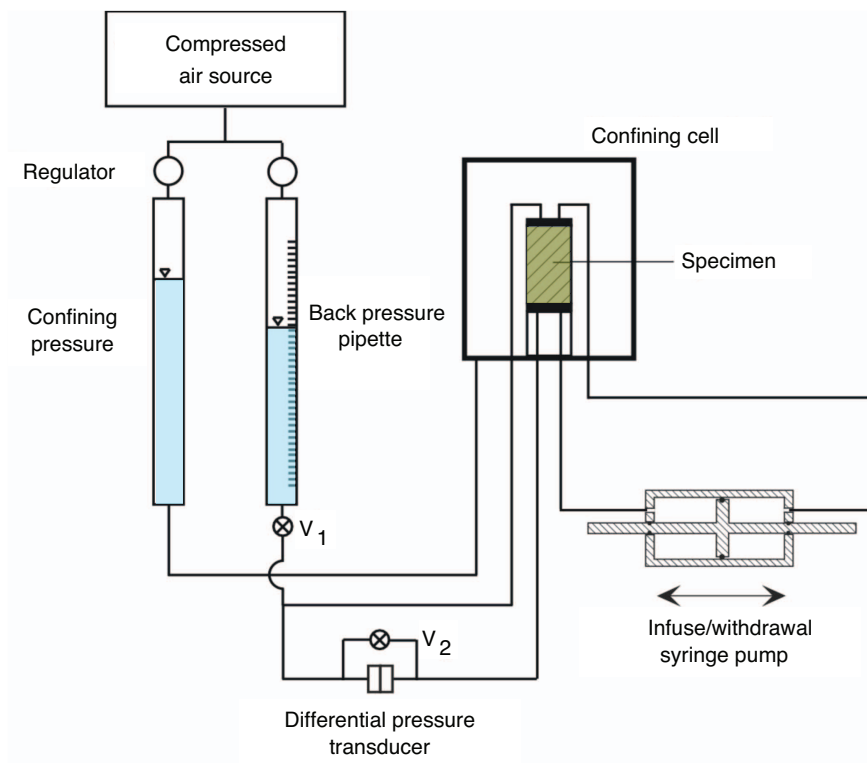
Figure F3. Schematic of testing system for constant-flow permeability at the University of Missouri (USA).

Figure F4. Example of typical responses of transient head difference (Δh_s) during flow-through testing. Q = volumetric flow rate, K = hydraulic conductivity.

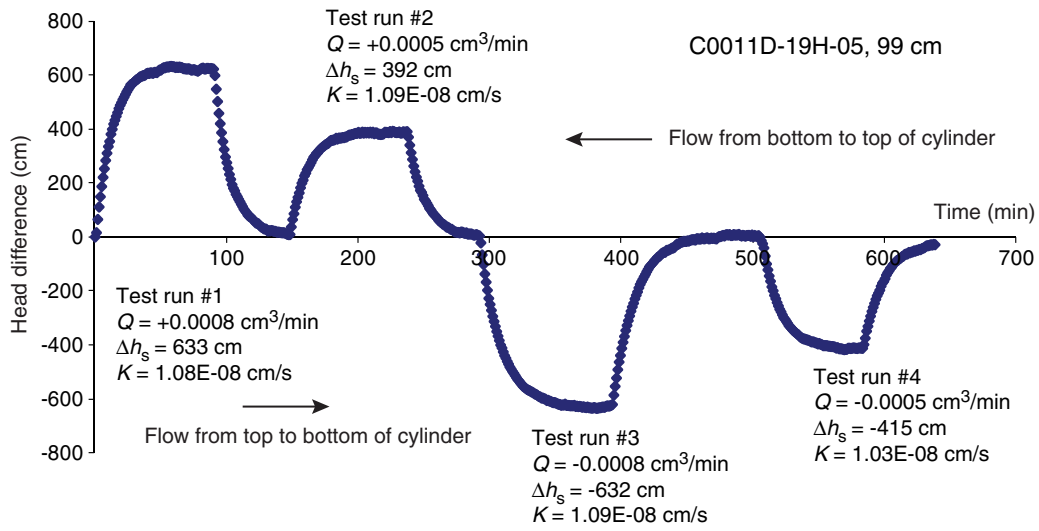


Figure F5. Geometric relations among bedding, orientation of the core axis, and the horizontal and vertical sections used for imaging by environmental scanning electron microscope.

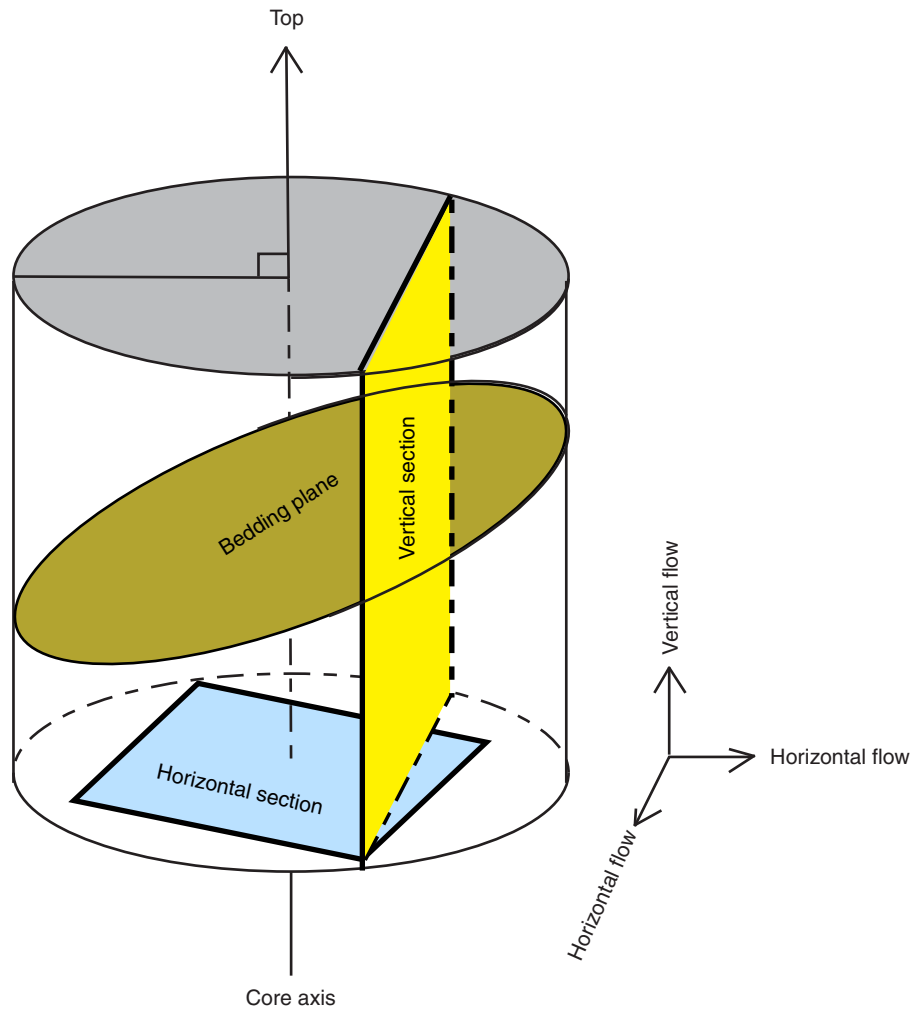


Figure F6. Environmental scanning electron microscope images for all specimens tested for permeability, Sites C0011 and C0012. Relative to the core axis, sections were cut parallel (vertical) and perpendicular (horizontal). See Figure F2 and Table T1 for bedding dips. (Continued on next two pages.)

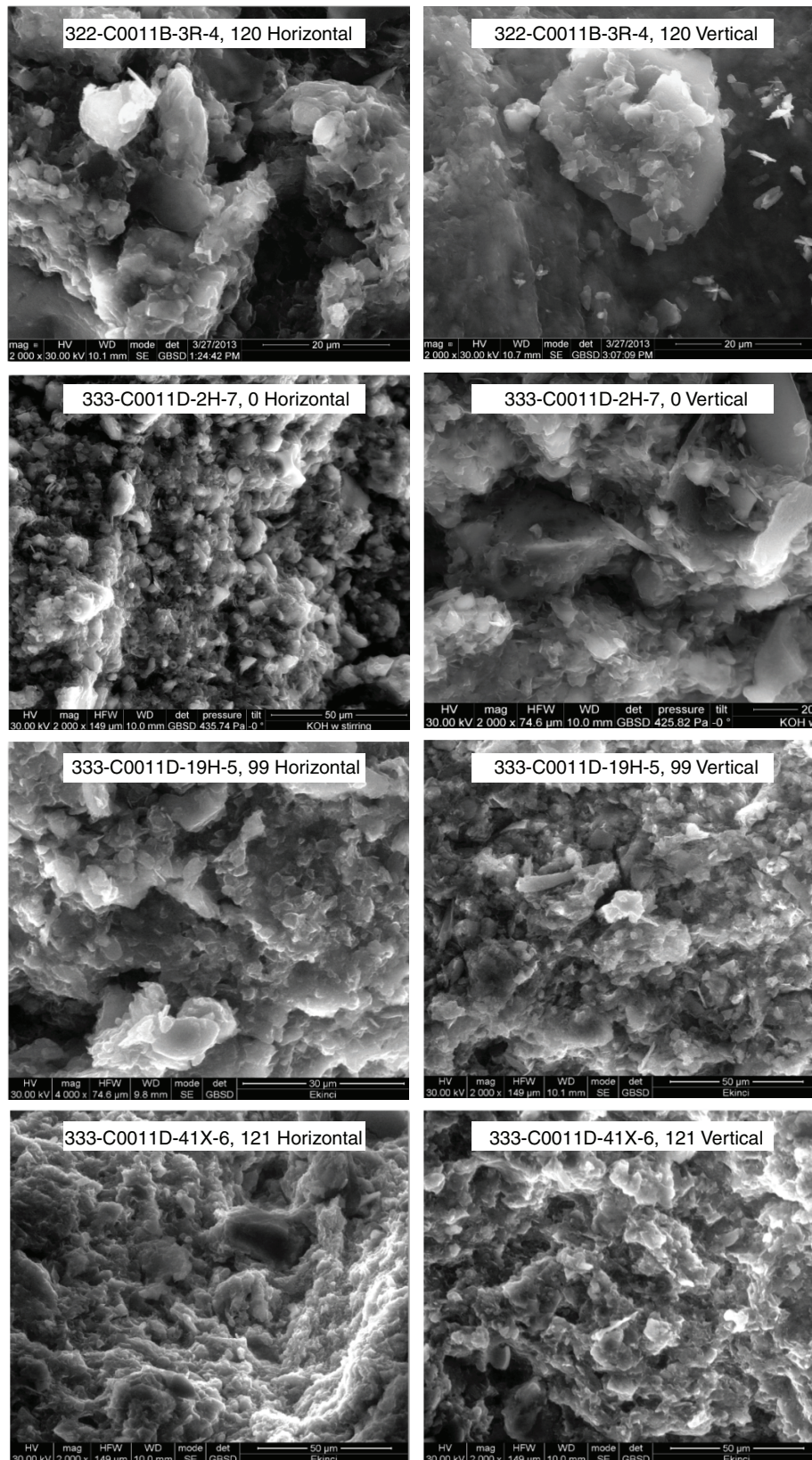


Figure F6 (continued). (Continued on next page.)

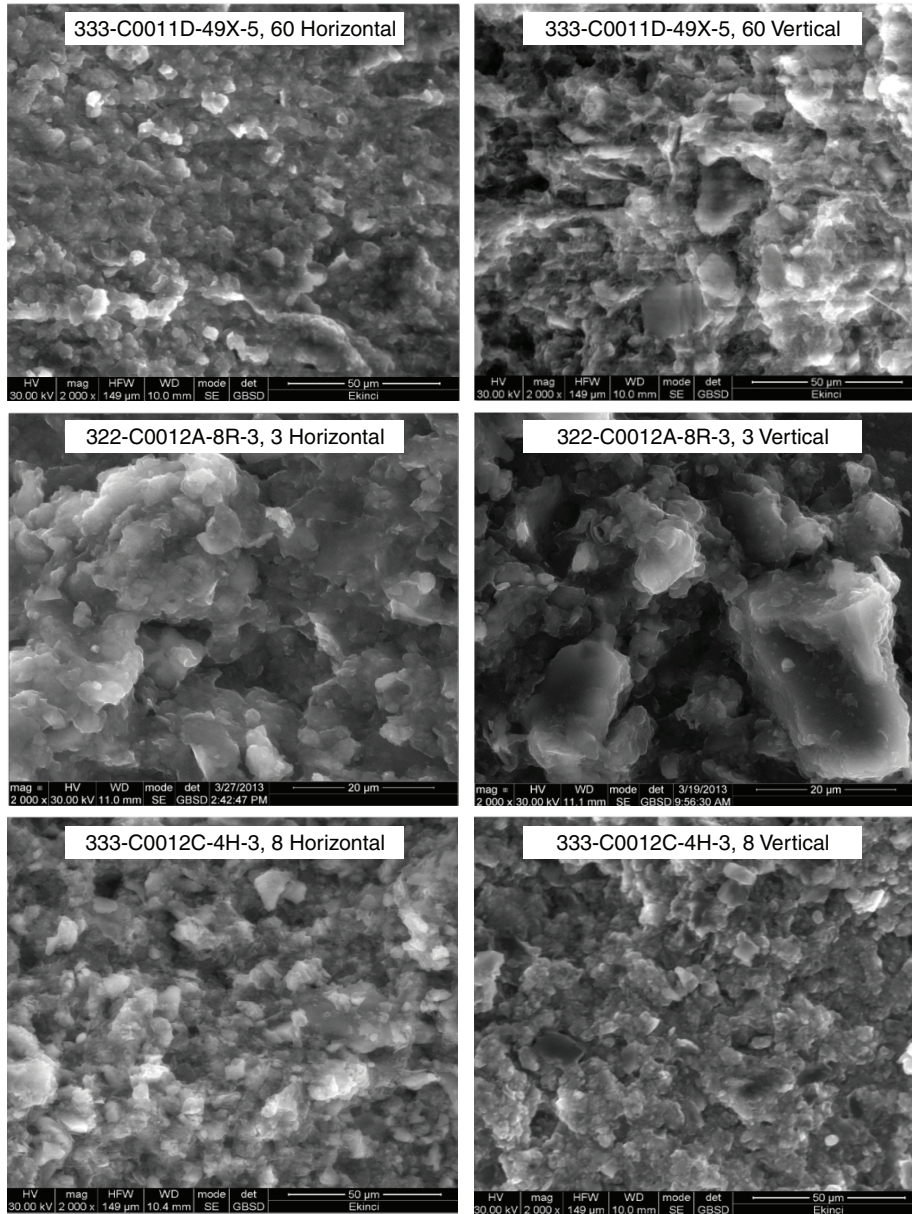


Figure F6 (continued).

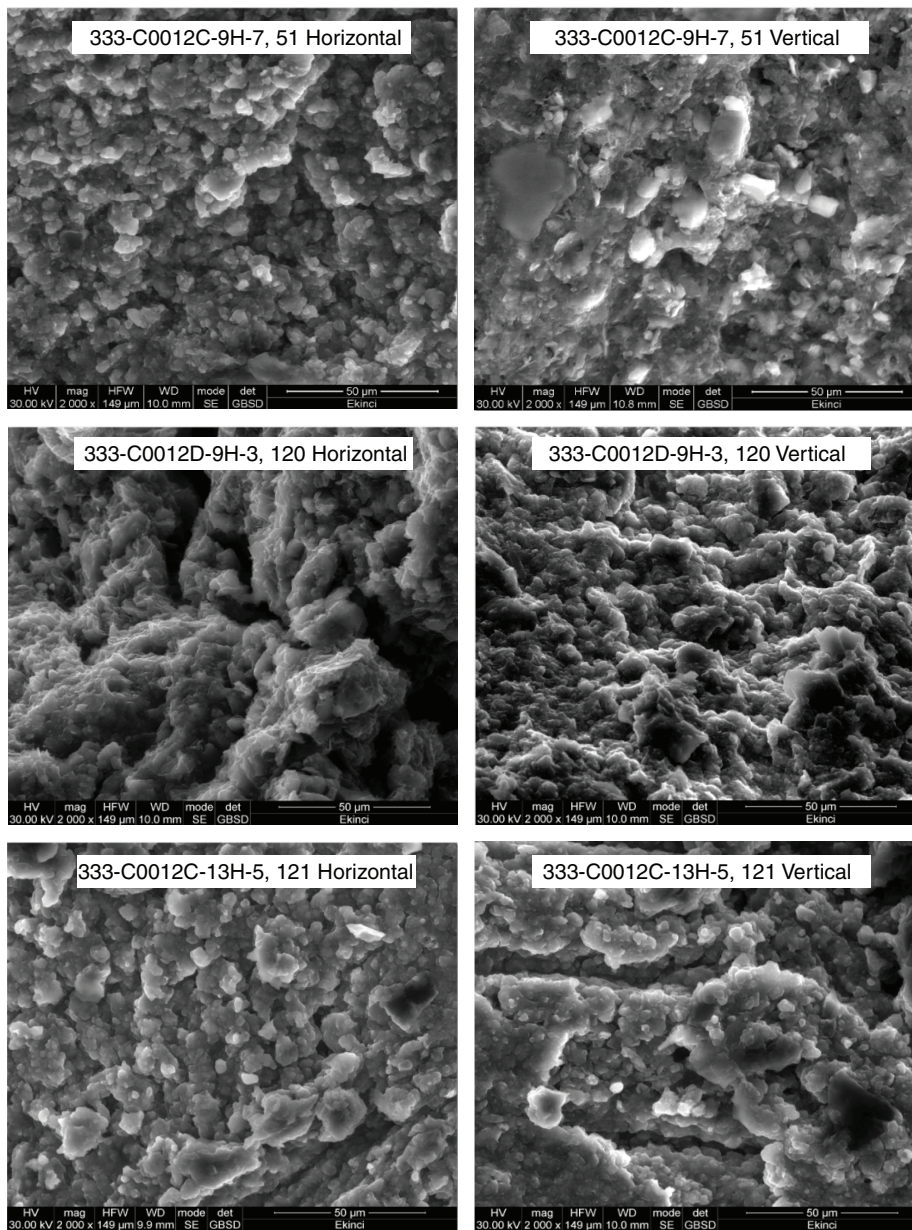


Figure F7. Values of intrinsic permeability (horizontal, vertical) vs. depth, Sites C0011 and C0012. Permeability was measured at an effective stress of 0.55 MPa.

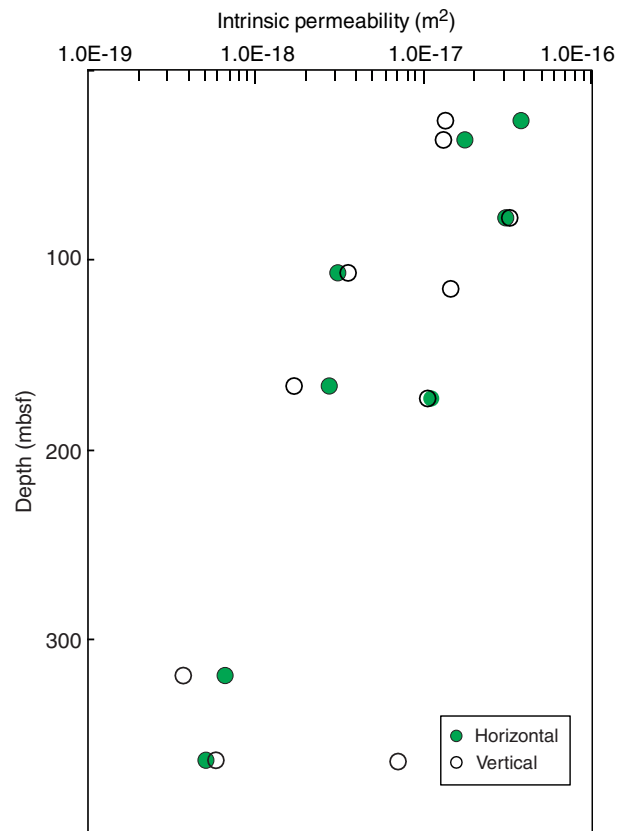


Figure F8. Relation between intrinsic permeability and post-test porosity for specimens, Sites C0011 and C0012.

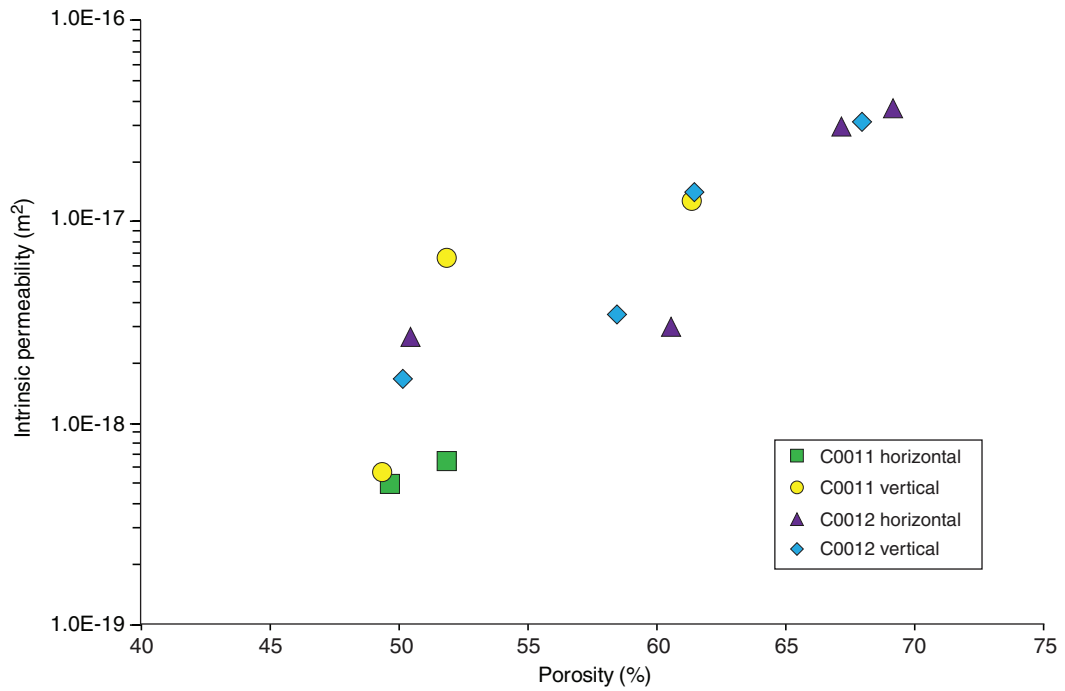


Figure F9. Orientation of grains (apparent long axis) measured on environmental scanning electron microscope (ESEM) images. Relative to the core axis, sections were cut parallel (vertical) and perpendicular (horizontal). See Figure F6 for the corresponding ESEM images. Also shown are values of standard deviation (d) for grain orientation, values of microfabric orientation index (i), values of resultant vector length (R), and the mean angle (α) of the angular distribution. (Continued on next page.)

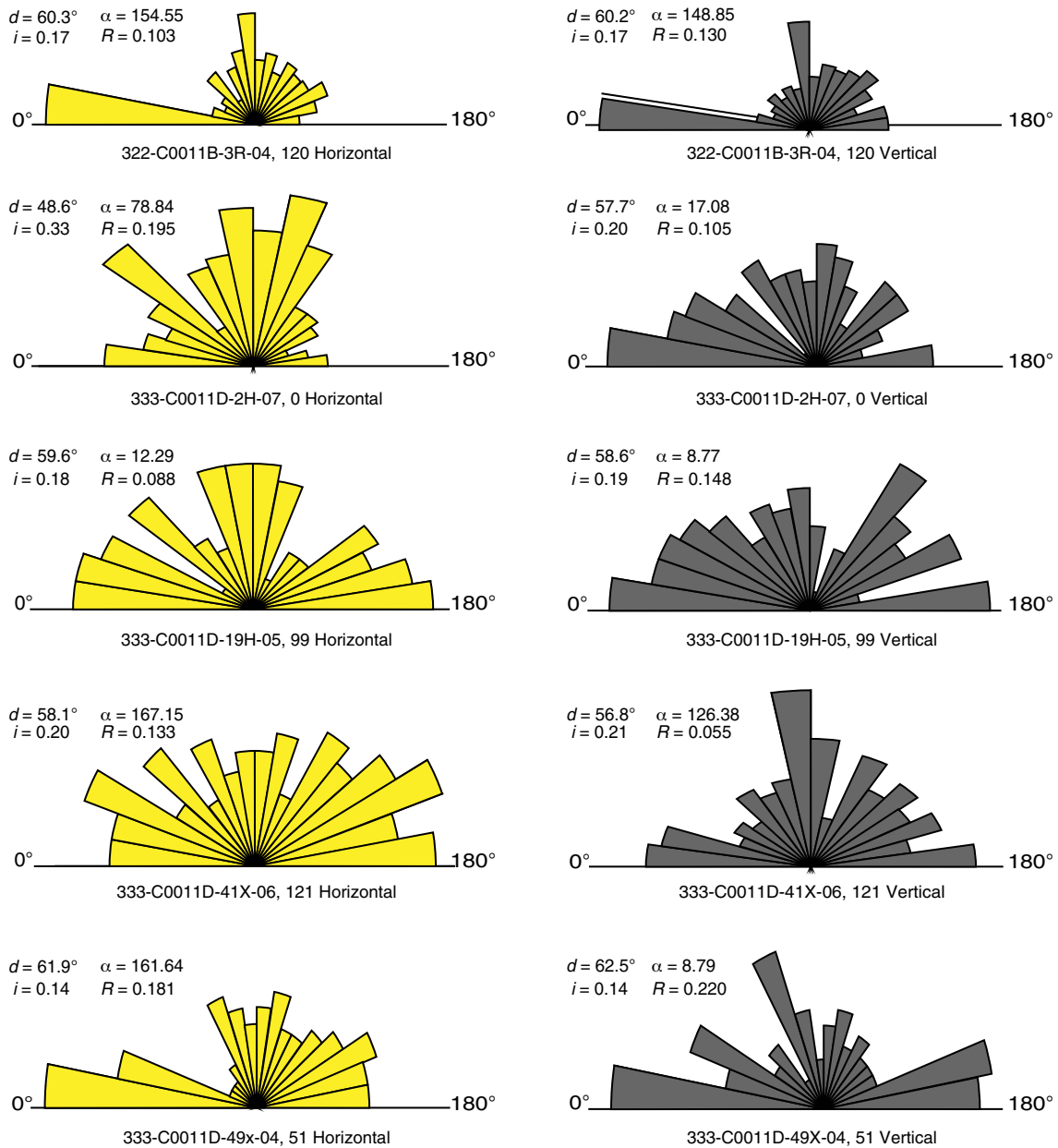
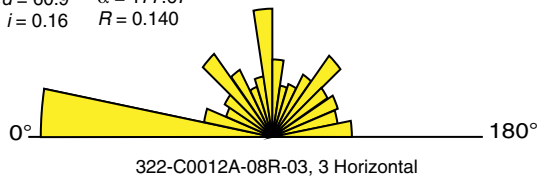
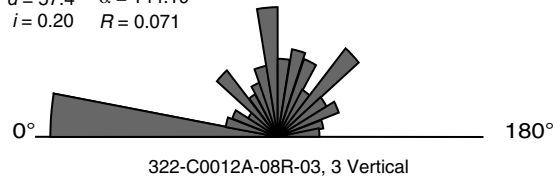


Figure F9 (continued).

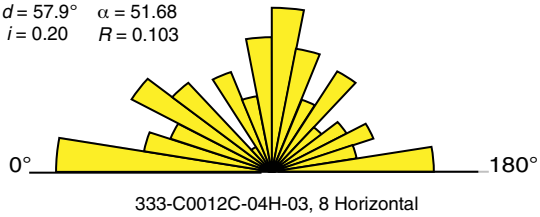
$d = 60.9^\circ$ $\alpha = 177.67$
 $i = 0.16$ $R = 0.140$



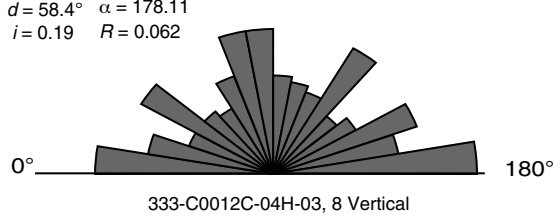
$d = 57.4^\circ$ $\alpha = 144.19$
 $i = 0.20$ $R = 0.071$



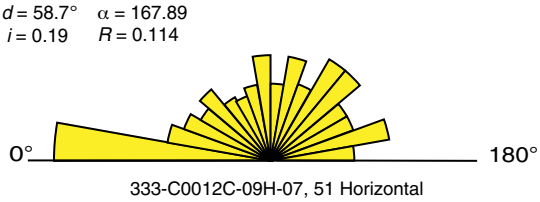
$d = 57.9^\circ$ $\alpha = 51.68$
 $i = 0.20$ $R = 0.103$



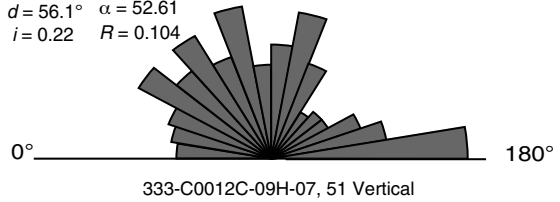
$d = 58.4^\circ$ $\alpha = 178.11$
 $i = 0.19$ $R = 0.062$



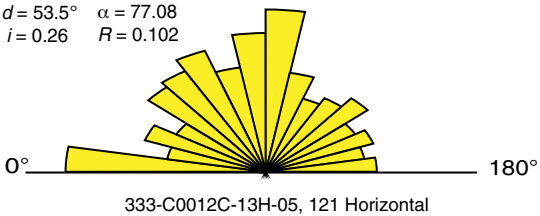
$d = 58.7^\circ$ $\alpha = 167.89$
 $i = 0.19$ $R = 0.114$



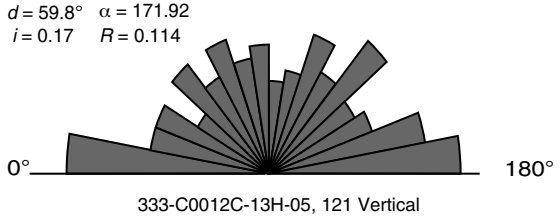
$d = 56.1^\circ$ $\alpha = 52.61$
 $i = 0.22$ $R = 0.104$



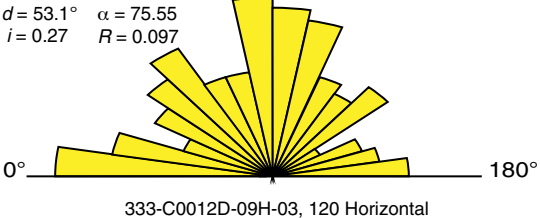
$d = 53.5^\circ$ $\alpha = 77.08$
 $i = 0.26$ $R = 0.102$



$d = 59.8^\circ$ $\alpha = 171.92$
 $i = 0.17$ $R = 0.114$



$d = 53.1^\circ$ $\alpha = 75.55$
 $i = 0.27$ $R = 0.097$



$d = 61.8^\circ$ $\alpha = 166.20$
 $i = 0.15$ $R = 0.319$

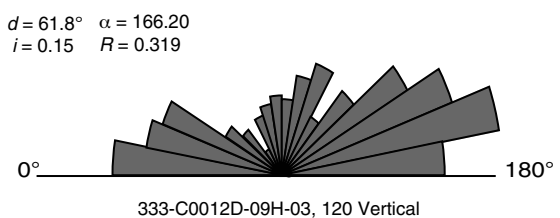


Figure F10. Cumulative frequency curves for grain orientations on horizontal sections (perpendicular to core axis) and vertical sections (parallel to core axis) imaged by environmental scanning electron microscope, Sites C0011 and C0012.

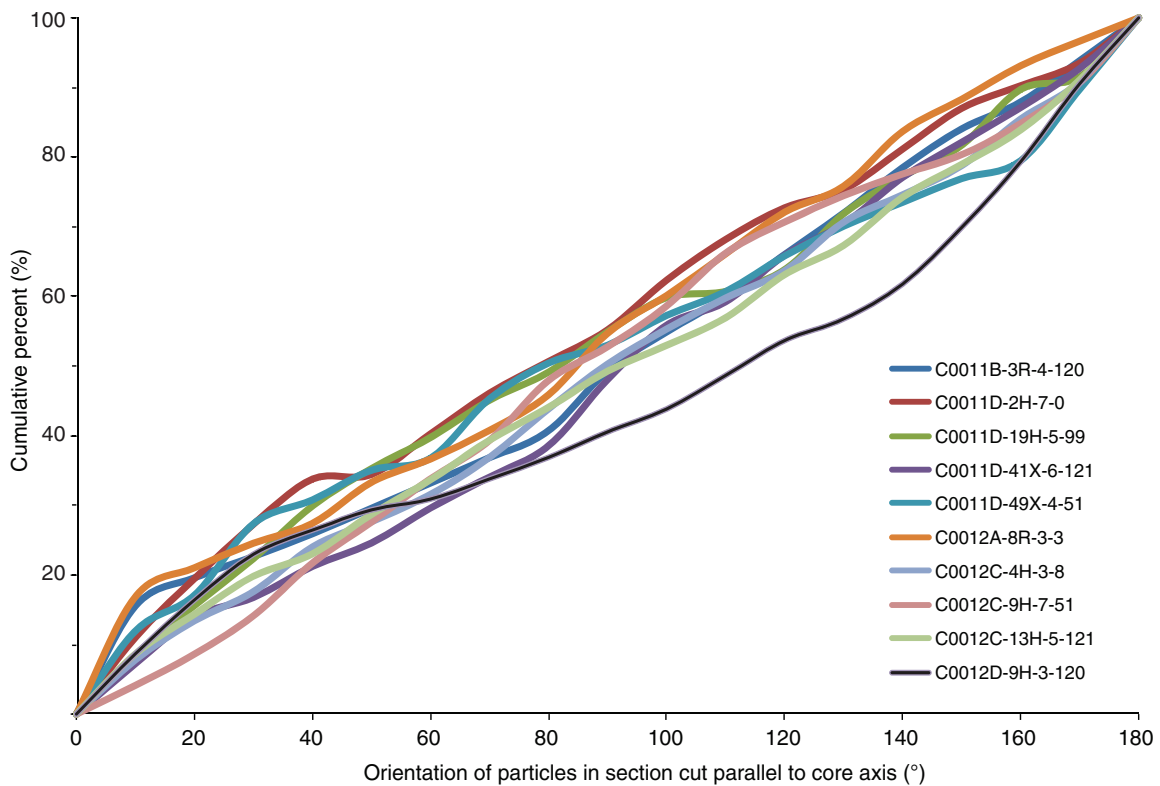
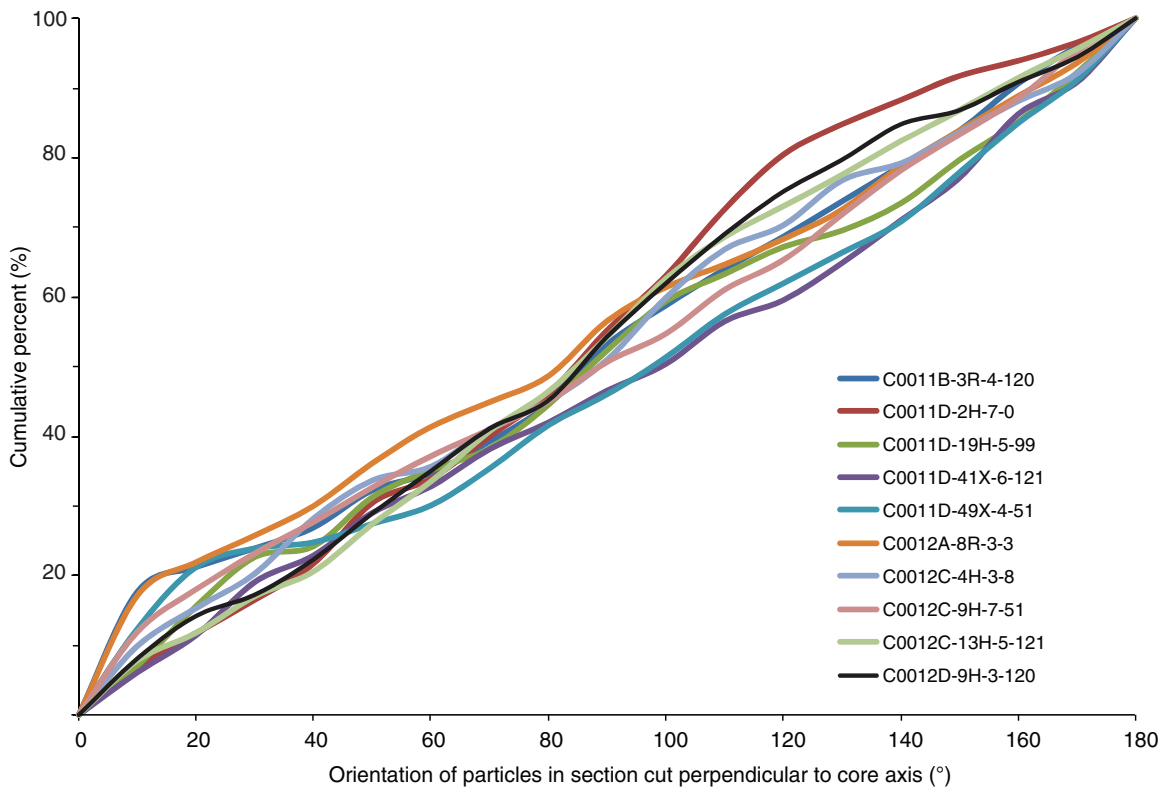


Figure F11. Depth-dependent trends in the index of orientation (for horizontal and vertical sections) and the anisotropy of permeability (k_h/k_v), Sites C0011 and C0012.

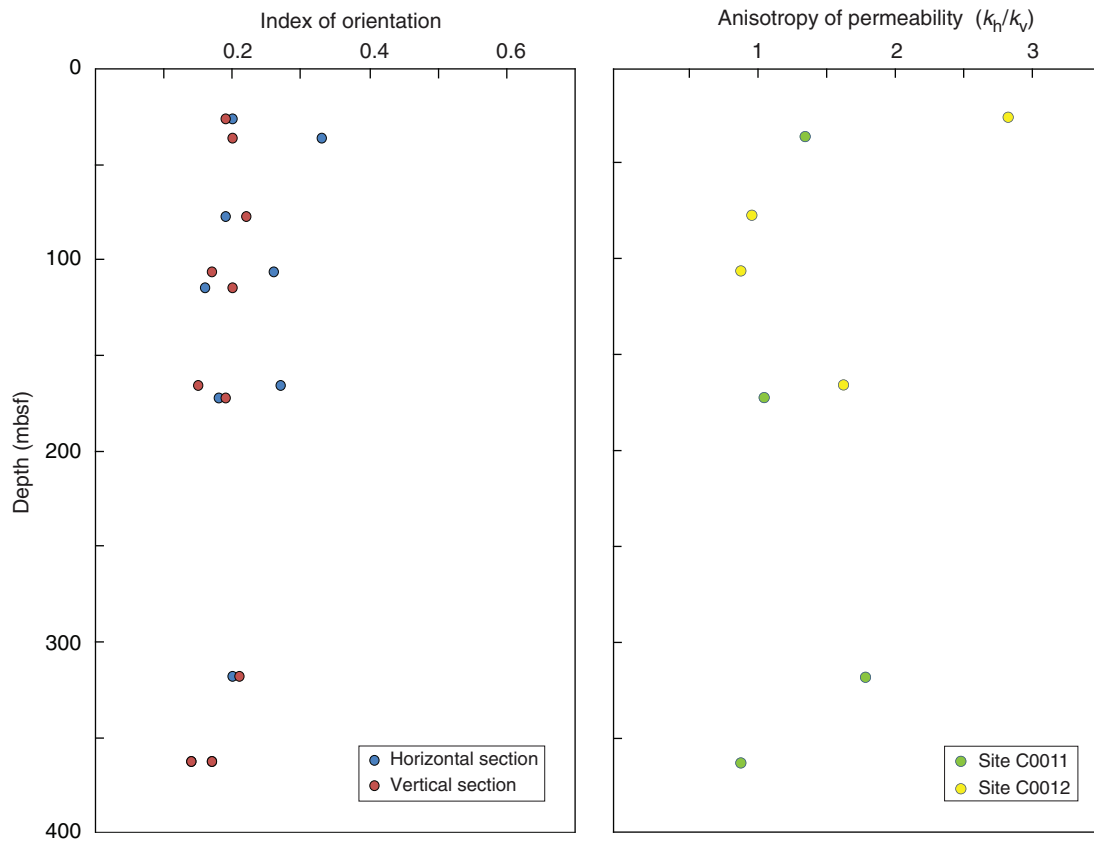



Table T1. Summary of specimen properties before and after flow-through permeability tests, Sites C0011 and C0012.

Core, section, interval (cm)	Lith. unit	Top depth (mbsf)	Bedding dip (°)	Cylinder orientation	Avg. height (cm)	Avg. diameter (cm)	Skempton <i>B</i> -value	Shipboard data		Before test		After test	
								Grain density (g/cm ³)	Porosity (%)	Water content (%)	Porosity (%)	Water content (%)	Porosity (%)
322-C0011B-													
3R-4, 120–140	II	362.58	14	Vertical	6.30	4.11	1.00	2.74	62	42	53	40	52
19R-6, 0–19	III	495.61	7	Trim failed				2.72	44				
51R-2, 122–136	IV	748.62	4	Trim failed				2.61	40				
333-C0011D-													
2H-07, 0–20	I	36.23	5	Horizontal	5.37	3.67	0.95	2.49	61	63	63		
2H-07, 0–20	I	36.23	5	Vertical	5.83	3.84	0.92	2.49	61			59	61
19H-5, 99–115	I	172.32	27	Horizontal	5.39	3.77	0.95	2.73	67				
19H-5, 99–115	I	172.32	27	Vertical	6.50	4.01	0.96	2.73	67	64	64		
32X-6, 24–53	I	246.03	16	Trim failed				3.05	69				
41X-6, 121–141	I	317.99	12	Horizontal	3.15	4.00	0.87	2.72	52	44	54	40	52
41X-6, 121–141	I	317.99	12	Vertical	6.98	3.84	0.95	2.72	52				
49X-4, 51–67	II	362.58	10	Horizontal	3.49	4.12	0.89	2.68	52	34	48	37	50
49X-4, 51–67	II	362.58	10	Vertical	7.03	5.84	0.96	2.68	52	47	56	36	49
322-C0012A-													
8R-3, 32–47	I	114.63	4	Vertical	7.11	4.31	0.81	2.69	63	56	60	59	61
17R-2, 19–34	II	198.39	3	Test failed				2.48	49				
31R-4, 46–64	III	331.53	12	Trim failed				2.85	49				
333-C0012C-													
4H-3, 8–27	I	26.22	60	Horizontal	5.07	4.04	0.95	2.72	74	97	72	84	69
4H-3, 8–27	I	26.22	60	Vertical	6.39	6.54	0.95	2.72	74	90	71		
9H-7, 51–70	I	77.33	63	Horizontal	5.50	4.30	0.81	2.62	67	78	68	76	67
9H-7, 51–70	I	77.33	63	Vertical	6.28	4.23	0.95	2.62	67	79	68	78	68
13H-5, 121–137	I	106.28	8–17	Horizontal	5.34	4.02	0.96	2.72	59	55	60	57	61
13H-5, 121–137	I	106.28	8–17	Vertical	6.45	4.30	0.97	2.72	59	53	59	52	58
333-C0012D-													
9H-3, 120–136	II	165.74	35	Horizontal	5.47	4.29	0.96	2.62	49	37	50	38	50
9H-3, 120–136	II	165.74	35	Vertical	6.45	4.30	0.97	2.62	49	38	50	37	50

Table T2. Results of individual flow-through permeability tests, Sites C0011 and C0012. Note that some tests failed because of a faulty pressure transducer. (Continued on next page.)

Core, section, interval (cm)	Test run	Volumetric flow rate (cm ³ /min)	Discharge velocity (cm/s)	Head difference (cm)	Hydraulic gradient	Hydraulic conductivity (cm/s)	Intrinsic permeability (m ²)
322-C0011B-							
3R-4, 120 vertical	1	0.00005	6.28E-08	331	52.54	2.39E-09	2.37E-18
	2	-0.00005	-6.28E-08	-339	-53.81	1.16E-08	1.15E-17
	3	0.00003	3.77E-08	136	21.59	2.33E-09	2.31E-18
	4	-0.00003	-3.77E-08	-142	-22.54	1.11E-08	1.10E-17
					Average:	6.86E-09	6.80E-18
333-C0011D-							
2H-07, 0 horizontal	1	-0.0005	-7.88E-07	-271	-50.47	1.56E-08	1.55E-17
	2	-0.0008	-1.26E-06	-402	-74.86	1.68E-08	1.67E-17
	3	0.0005	7.88E-07	218	40.60	1.94E-08	1.93E-17
	4	0.0008	1.26E-06	363	67.60	1.86E-08	1.85E-17
					Average:	1.76E-08	1.75E-17
2H-07, 0 vertical	1	0.001	1.44E-06	660	113.21	1.27E-08	1.26E-17
	2	0.0008	1.15E-06	520	89.19	1.29E-08	1.28E-17
	3	-0.001	-1.44E-06	-630	-108.06	1.33E-08	1.32E-17
	4	-0.0008	-1.15E-06	-501	-85.93	1.34E-08	1.33E-17
					Average:	1.31E-08	1.30E-17
19H-05, 99 horizontal	1	0.0008	1.19E-06	578	107.24	1.11E-08	1.10E-17
	2	0.0005	7.47E-07	353	65.49	1.14E-08	1.13E-17
	3	-0.0008	-1.19E-06	-582	-107.98	1.11E-08	1.10E-17
	4	-0.0005	-7.47E-07	-374	-69.39	1.08E-08	1.07E-17
					Average:	1.11E-08	1.10E-17
19H-05, 99 vertical	1	0.0008	1.06E-06	633	97.38	1.08E-08	1.07E-17
	2	0.0005	6.60E-07	392	60.31	1.09E-08	1.08E-17
	3	-0.0008	-1.06E-06	-632	-97.23	1.09E-08	1.08E-17
	4	-0.0005	-6.60E-07	-415	-63.85	1.03E-08	1.02E-17
					Average:	1.07E-08	1.06E-17
41X-06, 121 horizontal	1	0.00003	3.98E-08	200	63.49	6.27E-10	6.22E-19
	2	-0.00005	-6.63E-08	-304	-96.51	6.87E-10	6.82E-19
	3	-0.00003	-3.98E-08	—	—	—	—
	4	0.00005	6.63E-08	—	—	—	—
					Average:	6.57E-10	6.52E-19
41X-06, 121 vertical	1	0.00001	1.44E-08	303	43.41	3.32E-10	3.30E-19
	2	0.00002	2.88E-08	587	84.10	3.42E-10	3.39E-19
	3	-0.00001	-1.44E-08	-251	-35.96	4.00E-10	3.97E-19
	4	-0.00002	-2.88E-08	-495	-70.92	4.06E-10	4.03E-19
					Average:	3.70E-10	3.67E-19
49X-04, 51 horizontal	1	0.00005	6.25E-08	424	121.49	5.15E-10	5.11E-19
	2	0.00002	2.50E-08	176	50.43	4.96E-10	4.92E-19
	3	-0.0003	-3.75E-07	—	—	—	—
	4	-0.0005	-6.25E-07	—	—	—	—
					Average:	5.06E-10	5.02E-19
49X-04, 51 vertical	1	0.00005	3.11E-08	378	53.77	5.79E-10	5.75E-19
	2	0.0003	1.87E-07	—	—	—	—
	3	-0.00005	-3.11E-08	—	—	—	—
	4	-0.0003	-1.87E-07	—	—	—	—
					Average:	5.79E-10	5.75E-19
322-C0012A-							
8R-3, 3 vertical	1	0.0001	1.14E-07	131	18.45	1.58E-08	1.57E-17
	2	0.0002	2.29E-07	173	24.37	2.39E-08	2.37E-17
	3	-0.0001	-1.14E-07	-299	-42.11	6.92E-09	6.87E-18
	4	-0.0002	-2.29E-07	-365	-51.41	1.13E-08	1.12E-17
					Average:	1.45E-08	1.44E-17
333-C0012C-							
4H-03, 8 horizontal	1	0.001	1.30E-06	166	32.74	3.97E-08	3.94E-17
	2	0.003	3.90E-06	515	101.58	3.84E-08	3.81E-17
	3	-0.001	-1.30E-06	-182	-35.90	3.62E-08	3.59E-17
	4	-0.003	-3.90E-06	-525	-103.55	3.77E-08	3.74E-17
					Average:	3.80E-08	3.77E-17
4H-03, 8 vertical	1	0.001	4.96E-07	248	38.81	1.28E-08	1.27E-17
	2	-0.0005	-2.48E-07	-112	-17.53	1.42E-08	1.40E-17
	3	-0.001	-4.96E-07	—	—	—	—
	4	0.0005	2.48E-07	—	—	—	—

Table T2 (continued).

Core, section, interval (cm)	Test run	Volumetric flow rate (cm ³ /min)	Discharge velocity (cm/s)	Head difference (cm)	Hydraulic gradient	Hydraulic conductivity (cm/s)	Intrinsic permeability (m ²)
					Average:	1.35E-08	1.34E-17
9H-07, 51 horizontal	1	0.001	1.15E-06	206	37.45	3.06E-08	3.04E-17
	2	0.002	2.30E-06	410	74.55	3.08E-08	3.06E-17
	3	-0.001	-1.15E-06	-205	-37.27	3.08E-08	3.06E-17
	4	-0.002	-2.30E-06	-408	-74.18	3.09E-08	3.07E-17
					Average:	3.08E-08	3.06E-17
9H-07, 51 vertical	1	0.001	1.19E-06	224	35.67	3.32E-08	3.30E-17
	2	0.002	2.37E-06	462	73.57	3.22E-08	3.20E-17
	3	-0.001	-1.19E-06	-232	-36.94	3.21E-08	3.19E-17
	4	-0.002	-2.37E-06	-460	-73.25	3.24E-08	3.21E-17
					Average:	3.25E-08	3.23E-17
13H-05, 121 horizontal	1	0.0001	1.31E-07	220	41.20	3.19E-09	3.16E-18
	2	0.0002	2.63E-07	456	85.39	3.08E-09	3.05E-18
	3	-0.0001	-1.31E-07	-233	-43.63	3.01E-09	2.99E-18
	4	-0.0002	-2.63E-07	-460	-86.14	3.05E-09	3.03E-18
					Average:	3.08E-09	3.06E-18
13H-05, 121 vertical	1	0.0001	1.15E-07	203	31.47	3.65E-09	3.62E-18
	2	0.0002	2.30E-07	385	59.69	3.85E-09	3.82E-18
	3	-0.0001	-1.15E-07	-211	-32.71	3.51E-09	3.48E-18
	4	-0.0002	-2.30E-07	-465	-72.09	3.18E-09	3.16E-18
					Average:	3.55E-09	3.52E-18
333-C0012D-9H-03, 120 horizontal	1	0.0001	1.15E-07	198	36.20	3.19E-09	3.16E-18
	2	0.0002	2.31E-07	550	100.55	2.29E-09	2.28E-18
	3	-0.0001	-1.15E-07	—	—	—	—
	4	-0.0002	-2.31E-07	—	—	—	—
					Average:	2.74E-09	2.72E-18
9H-03, 120 vertical	1	0.0001	1.15E-07	350	54.26	2.12E-09	2.10E-18
	2	0.00008	9.18E-08	292	45.27	2.03E-09	2.01E-18
	3	-0.0001	-1.15E-07	-513	-79.53	1.44E-09	1.43E-18
	4	-0.00008	-9.18E-08	-502	-77.83	1.18E-09	1.17E-18
					Average:	1.69E-09	1.68E-18

Table T3. Statistics for mudstone microfabric calculated from analyses of environmental scanning electron microscope images, Sites C0011 and C0012.

Core, section, interval (cm)	Top depth (mbsf)	Horizontal section					Vertical section				
		Grains counted	Stand. dev. orientation (°)	Index of orientation	Mean angle (°)	Resultant vector length	Grains counted	Stand. dev. orientation (°)	Index of orientation	Mean angle (°)	Resultant vector length
322-C0011B-3R-4, 120	362.58	769	60.3	0.17	154.44	0.103	521	60.2	0.17	148.85	0.130
333-C0011D-2H-07, 0	36.33	230	48.6	0.33	78.84	0.195	154	57.7	0.2	17.08	0.105
19H-05, 99	172.32	128	59.6	0.18	12.29	0.088	224	58.6	0.19	8.77	0.148
41X-06, 121	317.99	131	58.1	0.2	167.15	0.133	179	56.8	0.21	126.38	0.055
49X-04, 51	362.58	113	61.9	0.14	161.64	0.181	117	62.5	0.14	8.79	0.220
322-C0012A-8R-3, 3	114.63	1013	60.9	0.16	177.67	0.140	1018	57.4	0.2	144.19	0.071
333-C0012C-4H-03, 8	26.22	202	57.9	0.2	51.68	0.103	358	58.4	0.19	178.11	0.062
9H-07, 51	77.33	444	58.7	0.19	167.89	0.114	290	56.1	0.22	52.61	0.104
13H-05, 121	106.28	704	53.5	0.26	77.08	0.102	404	59.8	0.17	171.92	0.114
333-C0012D-9H-03, 120	165.74	197	53.1	0.27	75.55	0.097	518	61.8	0.15	166.20	0.319

Table T4. Average values of permeability and hydraulic conductivity for horizontal and vertical test directions, Sites C0011 and C0012.

Core, section, interval (cm)	Top depth (mbsf)	Hydraulic conductivity (cm/s)		Intrinsic permeability (m ²)		k_h/k_v
		Horizontal	Vertical	Horizontal	Vertical	
322-C0011B-3R-4, 120	362.58		6.86E-09		6.80E-18	
333-C0011D-2H-07, 0	36.33	1.76E-08	1.31E-08	1.75E-17	1.30E-17	1.34
19H-05, 99	172.32	1.11E-08	1.07E-08	1.10E-17	1.06E-17	1.04
41X-06, 121	317.99	6.57E-10	3.70E-10	6.52E-19	3.67E-19	1.78
49X-04, 51	362.58	5.06E-10	5.79E-10	5.02E-19	5.75E-19	0.87
322-C0012A-8R-3, 3	114.63		1.45E-08		1.44E-17	
333-C0012C-4H-03, 8	26.22	3.80E-08	1.35E-08	3.77E-17	1.34E-17	2.82
9H-07, 51	77.33	3.08E-08	3.25E-08	3.06E-17	3.23E-17	0.95
13H-05, 121	106.28	3.08E-09	3.55E-09	3.06E-18	3.52E-18	0.87
333-C0012D-9H-03, 120	165.74	2.74E-09	1.69E-09	2.72E-18	1.68E-18	1.62

Appendix

Plots of hydraulic gradient versus discharge velocity are presented in Figures [AF1](#), [AF2](#), [AF3](#), [AF4](#), and [AF5](#).

Figure AF1. Plot of hydraulic gradient versus discharge velocity, Samples 322-C0011B-3R-4, 120 cm, and 333-C0011D-2H-7, 0 cm.

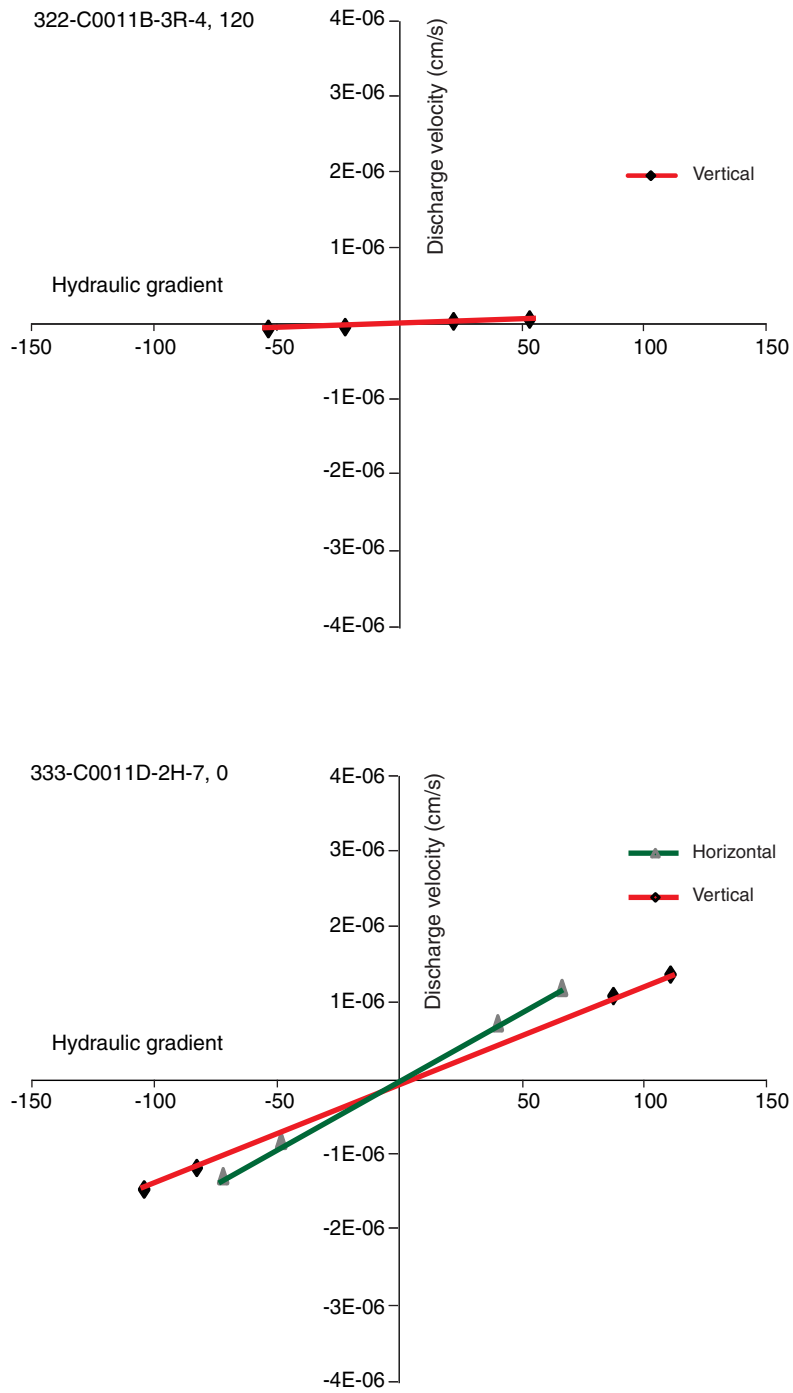


Figure AF2. Plot of hydraulic gradient versus discharge velocity, Samples 333-C0011D-19H-5, 99 cm, and 333-C0011D-41X-6, 121 cm.

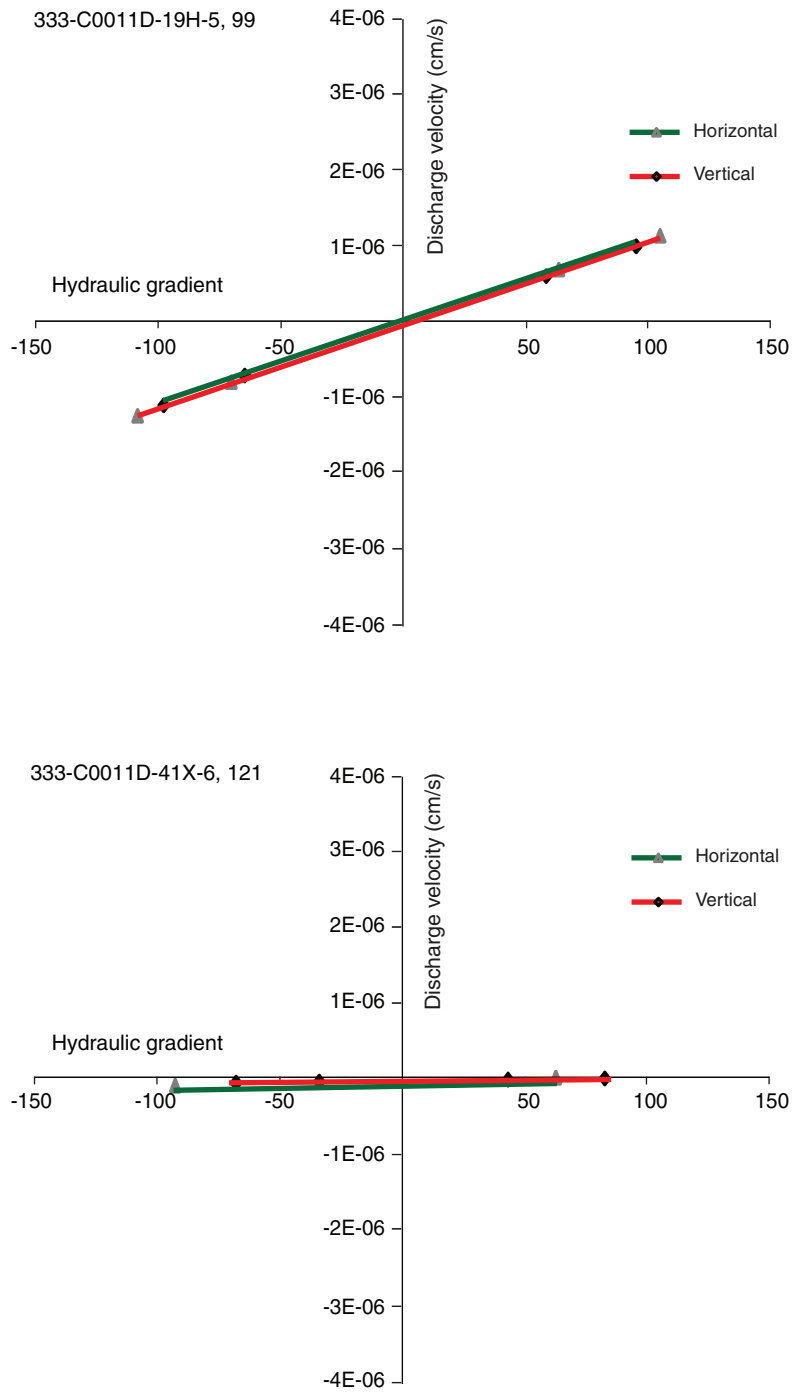


Figure AF3. Plot of hydraulic gradient versus discharge velocity, Samples 333-C0011D-49X-5, 60 cm, and 322-C0012A-8R-3, 3 cm.

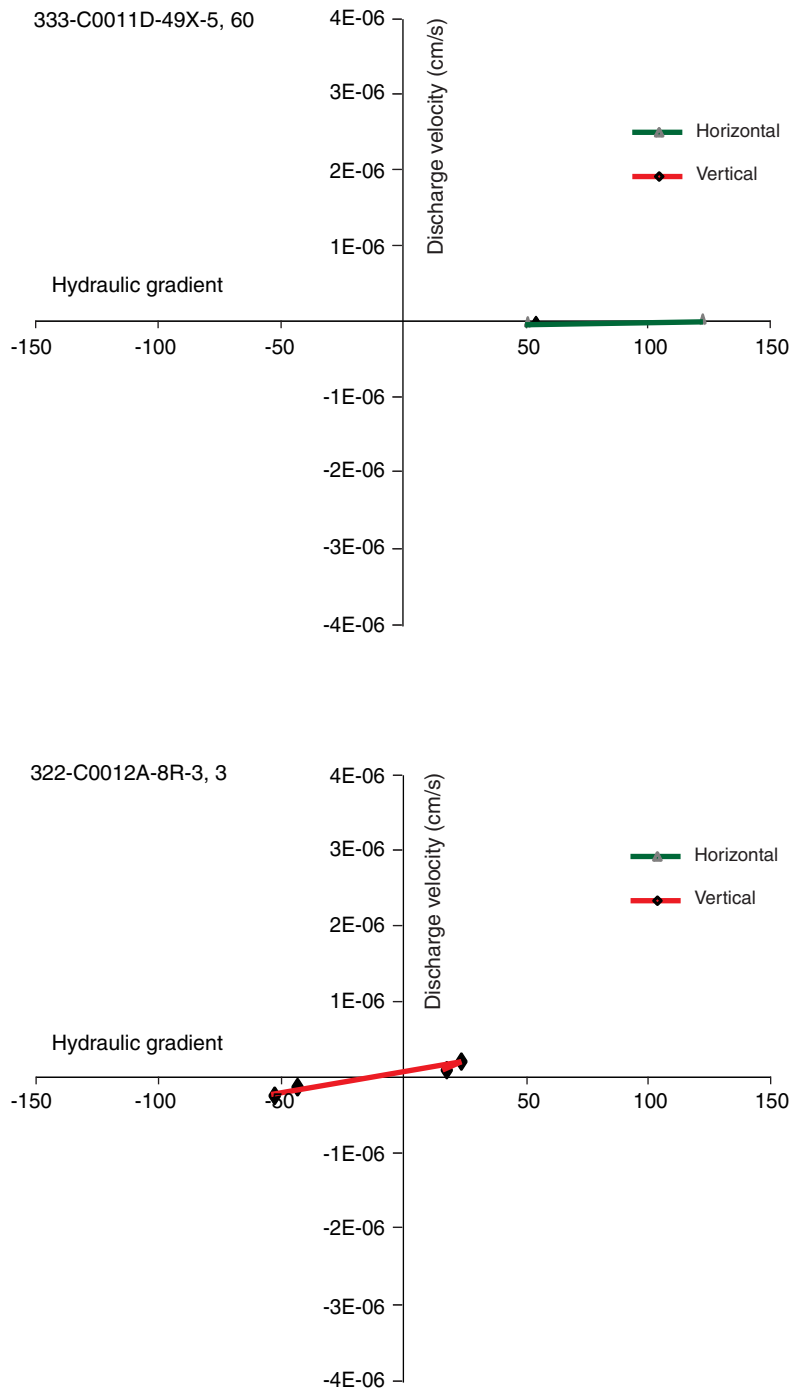


Figure AF4. Plot of hydraulic gradient versus discharge velocity, Samples 333-C0012C-4H-3, 8 cm, and 333-C0012C-9H-7, 51 cm.

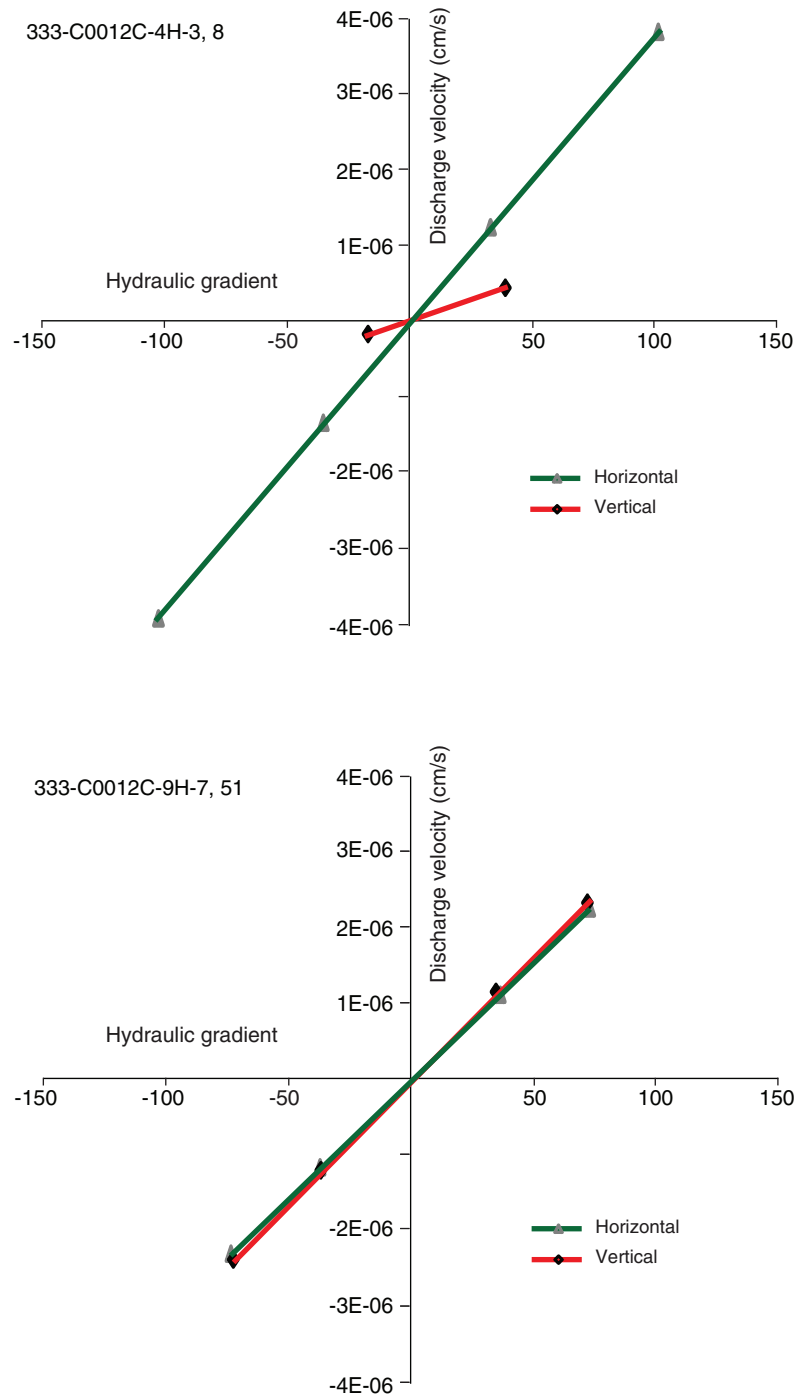


Figure AF5. Plot of hydraulic gradient versus discharge velocity, Samples 333-C--12C-13H-5, 121 cm, and 333-C0012D-9H-3, 120 cm.

